A combined first-principles and data-driven computational framework to analyze the surface structure, composition, and stability of binary alloy catalysts

Gaurav Deshmukh[1], Pushkar Ghanekar[1], Jeffrey Greeley[1*]

[1]Davidson School of Chemical Engineering, Purdue University, West Lafayette, IN 47907, USA

*Corresponding author: jgreeley@purdue.edu

1. Abstract

Pt-based bimetallic alloys are considerably more active than Pt for the oxygen reduction reaction (ORR). This increased activity has been attributed to weakening of the adsorption of ORR intermediates due to the presence of Pt "skins." Density functional theory (DFT) calculations have, in turn, pointed to the importance of surface segregation energies and Pt leaching on the formation and stability of the skins on close-packed surfaces of Pt alloys. The generalizability of these insights across different chemical environments, surface compositions, and facets, however, remains a subject of active research and is the focus of this work. We present a generalized computational framework combining DFT calculations and data-driven methods to predict the stability of different Pt_3X (X = Ni, Co, Fe, and Cu) alloy facets under vacuum conditions and in the presence of an electrochemical environment, wherein we analyze the combined effect of segregation, intrasurface phase separation, leaching, and surface oxidation as a function of electrode potential. The analysis reveals that a subtle interplay of these factors influences Pt skin formation and stability, with Pt segregation being a strong function of the surface structure, and continuous base metal dissolution being thermodynamically, although not always kinetically, favored at ORR-relevant voltages.

2. Introduction

Alloys are used as catalysts for a diverse range of electrochemical reactions such as hydrogen evolution[1], oxygen reduction[2], CO_2 electroreduction[3], methanol electrooxidation[4,5], and many others. Among these, the oxygen reduction reaction (ORR), which occurs at the cathode of a fuel cell, is a particularly challenging reaction to catalyze, not only due to its sluggish kinetics, but also due to a reaction environment that is highly corrosive (in an acidic medium) and oxidizing, leading to rapid catalyst degradation. Pt-based alloy catalysts have shown greater activity for the ORR compared to the commercially used Pt/C catalyst[2,6], and Pt_3Ni, in particular, is the current state-of-the-art[7–11]. However, the stability of Pt_3Ni in an electrochemical environment remains a critical issue that poses a significant barrier to its practical application. This stability is a function of surface structure and composition[2,7,12], which can be modified via various mechanisms including surface segregation[13,14], leaching[12,15–19], and adsorbate-induced surface processes such as surface oxidation[20,21]. Stamenkovic et al.[7] have demonstrated that these mechanisms also influence the activity of Pt_3Ni extended surfaces, as evidenced by the higher activity shown by the so-called "Pt skin" surfaces on Pt_3Ni, which have a Pt-rich top layer and an Ni-rich subsurface layer. Computational studies[2,22] have, in turn, suggested that the increase in activity results from a weakening of the binding of oxygen—compared to pure Pt—on such Pt skin surfaces. Nevertheless, incomplete understanding of the complex array of physico-chemical phenomena that affect the structure, activity, and stability of Pt_3Ni alloys motivate further studies of these phenomena, with an ultimate goal of suggesting strategies to design more stable Pt-based alloy catalysts for the ORR.

Over the past 25 years, a series of computational studies have begun to illuminate some of the phenomena described above. The celebrated density functional theory (DFT) studies of segregation in binary alloys by Nørskov and coworkers[14,23] involved calculation of segregation energies through atom exchange between different layers in a surface slab. These studies demonstrated that the segregation energy to move a Pt atom to the top layer from the subsurface layer in Pt_3Ni is negative, hence indicating the favorability of Pt segregation to the surface. A limited number of studies have also considered segregation in the presence of adsorbates such as oxygen. Ma & Balbuena[24] analyzed segregation with

low oxygen coverages on the alloy surfaces. Dapeng et al.[21] constructed a surface phase diagram based on an *ab initio* atomistic thermodynamics framework[25,26], determining that the Pt skin surface changes to an Ni-skin surface with ½ ML adsorbed oxygen atoms at higher oxygen chemical potentials; this conclusion was also supported by experimental studies[27,28] showing the propensity for O-induced segregation of Ni to the surface and subsequent oxidation of nickel in an oxygen-rich gas phase environment. Ma & Balbuena[18] also analyzed leaching of Pt_3Ni under electrochemical conditions—by applying the thermodynamic formalism developed by Greeley & Nørskov[17]—and calculated the dissolution potentials of Pt from the Pt skin layer, with and without oxygen adsorbates, which were found to be more positive compared to pure Pt. A limited number of studies have also looked at Pt-Ni ordering at longer length scales using potential functions trained on DFT calculations. Mueller and coworkers[29,30] performed a comprehensive analysis of the Pt_3Ni (111) surface using cluster expansion-based grand canonical Monte Carlo simulations and generated detailed phase maps to describe equilibrium surface composition profiles and correlate them with ORR activity. More recently, Hansen and coworkers[31,32] utilized machine learning-based methods to identify surface patterns on Pt-Ni nanoalloys.

In this work, we seek to extend the first principles treatments described above by introducing a generalized thermodynamic framework that (1) accounts for all possible structural and compositional perturbations at the surface and (2) provides a comprehensive picture of thermodynamic stability in both chemical and electrochemical environments by incorporating the combined influence of physico-chemical mechanisms such as segregation, leaching, intrasurface phase separation, and adsorbate-induced surface processes. The atomistic slab models used in the framework are developed for several Miller Index surface facets and consist of two regions—a fixed and ordered bulk region and a variable surface region with a specified number of active layers that is systematically populated with all possible surface compositions and configurations.

DFT calculations are employed to evaluate the energies of the above structures, and a canonical surface phase diagram, consisting of a one dimensional convex hull formalism, is then used to determine the thermodynamically stable surface compositions and configurations. The chemical potentials of these

configurations are next determined to identify surface compositions in equilibrium with the fixed bulk composition. Subsequently, a grand canonical surface phase diagram is constructed to determine the compositional and configurational evolution of the surface as a function of electrode potential in an electrochemical environment. The effect of leaching is considered by assuming an equilibrium between non-precious metals in the surface and their ions in solution. Finally, the influence of adsorbate-induced surface processes, such as surface oxidation, is incorporated using the computational hydrogen electrode (CHE)[33] method.

We use this framework to examine stability trends of Pt_3Ni and other bimetallics such as Pt_3Fe, Pt_3Co, and Pt_3Cu. We look at four facets of each of the alloys—(111), (100), (110), and (211)—to determine the structure sensitivity of these trends. To deal with the explosion in configuration space due to the inclusion of disordered configurations of the (211) facet, we use an active learning scheme to reduce the number of DFT evaluations required to accurately sample the search space. Beginning with training dataset of DFT calculations, we use the Monte-Carlo dropout[34] technique in a dropout graph convolutional network (dGCN)[35], based on the crystal graph convolutional neural network (CGCNN) framework developed by Xie et al.[36], to estimate uncertainty in target property predictions, and then use a thermodynamic criterion—based on the lower confidence bound (LCB) acquisition function[37]—to sample structures for further DFT evaluations.

Through a canonical analysis, we show that Pt skin formation is favored under vacuum for the (111) facet, although intrasurface phase segregation is not observed, consistent with previous experiments and computational studies. However, this favorability towards Pt-segregation is reversed for the (110) facet, as we observe Ni to be more stable in the top layer. We show that this is due to a surface coordination effect—Pt prefers to segregate to the surface site with a higher coordination number (CN) first—and that this effect is consistent across facets, most notably on the (211) facet, which has the most heterogeneous coordination environment.

Lastly, through a grand canonical analysis, we show that the leaching of Ni dominates over its surface oxidation (via OH and O adsorption), leading to the formation of a Pt-rich surface above $0\,V_{SHE}$. However, the difference between the driving forces for leaching and surface oxidation is reduced for

the (211) facet, which binds oxygen-containing adsorbates strongly. We close by discussing the potential role of kinetics in determining the surface composition profile.

3. Methods

3.1 Electronic Structure Calculations

Periodic density functional theory calculations in the Vienna Ab-Initio Simulation Package (VASP)[38] are used to perform electronic structure calculations. The Kohn-Sham orbitals are expressed in terms of a plane-wave basis set with an energy cutoff of 400 eV. The Perdew-Burke-Ernzerhof (PBE)[39] functional within the generalized gradient approximation (GGA) is used to model exchange and correlation effects. The Brillouin zone is sampled with a $4 \times 4 \times 1$ grid chosen according to the Monkhorst-Pack[40] scheme; the associated k-point density changes only slightly across different considered surfaces. Core electron states are expressed using the projector augmented wave (PAW)[41] method. Electron states above the Fermi level are populated at 0 K using the first-order Methfessel-Paxton[42] smearing scheme with a width of 0.2 eV. All the calculations are spin polarized. Geometric optimization of the surface structures is carried out until the Hellman-Feynman forces are below 0.02 eV/Å.

Lattice constants of Pt_3Ni, Pt_3Co, Pt_3Fe, and Pt_3Cu are calculated by relaxing the bulk unit cell volume. Values for the lattice constants are given in **Table S3**. The (111), (100) and (110) facets are modeled as $2 \times 2 \times 6$ unit cells, whereas the (211) facet is modeled as a $3 \times 2 \times 6$ unit cell with 15 Å of vacuum separating periodic images in the z-direction.

3.2 High-Throughput Workflow

The stoichiometric surfaces of all facets are generated from bulk alloy structures using the Python Atomic Simulation Environment (ASE)[43], and further modifications to the structures are performed using an in-house code. The top two layers of the alloy surfaces are designated as active layers, and these layers are systematically perturbed in terms of stoichiometry and arrangement such that all possible surface configurations are sampled. Out of this total set, unique configurations are sampled using structure matching tools from Pymatgen,[44] and only these unique geometries are used in the DFT

calculations. For each of the (100), (110) and (211) facets, two surface terminations exist, based on where the bulk is cleaved. We consider both terminations in our structure generation routine. We also build analysis tools to capture detailed characteristics of the surface structures, such as the number of atoms of each type in every layer, as well as the number of different types of bonds between atoms in the active layers. These statistics are later used to determine thermodynamic excess surface quantities.

We further couple our high-throughput structure generation, calculation, and analysis workflow with a machine learning-based surrogate model to reduce computational overhead in the case of the (211) facet, where the number of total configurations is about an order of magnitude higher the other three facets combined. Specifically, we train a dropout graph convolutional network (dGCN)[45]—based on the crystal graph convolutional neural network (CGCNN) framework developed by Xie et al.[46], additionally modified to include the coordination number of each atom as a node feature—on the DFT predictions of all the configurations of the (111), (100), and (110) facets, as well as a subset of the total number of (211) configurations. To quantify uncertainty in the predictions of the target property, we use a Monte-Carlo dropout scheme. This trained dGCN model is then used to predict the energies of all possible (211) configurations. We apply a thermodynamic stability criterion, involving the lower confidence bound (LCB) acquisition function, on the predicted target properties and uncertainties, and sample a subset for which we perform further DFT calculations.

3.3 Thermodynamic Formalism

Thermodynamic analyses are performed in the canonical and grand canonical ensembles. The former predicts stability for given compositions, whereas the latter describes an electrochemical environment as a function of electrode potential. The analyses are discussed primarily in the context of Pt_3Ni, but they can be generalized to other Pt_3X alloys considered in this work. Extensive quantities with a prime ($'$) are excess quantities, and those without a prime are rescaled excess quantities.

3.3.1 Canonical ensemble

An alloy model with a fixed bulk region (consisting of ordered Pt_3Ni) and a surface region with a specific number of active layers is considered. The surface region is allowed to access any composition, ranging from pure Pt to pure Ni, and any arrangement of Pt and Ni atoms. The rescaled excess

Helmholtz free energy (f_s) of this model is expressed as a function of the rescaled surface excess quantity of Pt (Γ_{Pt}), the surface energy (γ_s), and the surface chemical potentials of Pt (μ_{Pt}) and Ni (μ_{Ni}) using **Equation 1**, which is derived from the fundamental equation of thermodynamics:

$$f_s = \gamma_s + \mu_{Ni} + (\mu_{Pt} - \mu_{Ni})\Gamma_{Pt} \quad (1)$$

The rescaling procedure effectively sets the references for the surface excess free energy to structures with pure Pt and Ni surfaces and Pt_3Ni bulk substrates, and normalizes the surface excess values such that they lie between 0 and 1. Therefore, Γ_{Pt} is analogous to a surface composition, such that $\Gamma_{Pt} = 1$ represents a pure Pt surface and $\Gamma_{Pt} = 0$ represents a pure Ni surface on a Pt_3Ni bulk substrate. f_s, which is the free energy of a surface with a given Γ_{Pt} on a Pt_3Ni bulk substrate, involves two contributions—the energy required to transfer the requisite number of Pt and Ni atoms from reservoirs with chemical potentials μ_{Pt} and μ_{Ni} having pure Pt and pure Ni surfaces on Pt_3Ni bulk, respectively, and the surface energy. While the first contribution has an analog in standard bulk Helmholtz free energy expressions, the latter is exclusive to our formalism. A more detailed derivation is provided in **Section S1**.

In a procedure analogous to that used to generate bulk binary alloy phase diagrams[47,48], a canonical surface phase diagram is made by plotting f_s, calculated using DFT, against Γ_{Pt}, and a convex hull is used to determine phase stability. Configurational entropy is incorporated into the calculation of f_s through a Boltzmann average over all possible surface arrangements (see **Section S3**). The surface chemical potentials differences between Pt and Ni are obtained from the slopes of the convex hull. Consistent with the rescaling discussed above, these chemical potentials are referenced to the chemical potentials of the pure Pt and pure Ni surfaces on Pt_3Ni bulk, respectively. Separate convex hulls are constructed for 0 K and finite temperatures.

The formalism described above is valid when the number of active layers in the surface region is fixed, implying that $\Gamma_{Pt} + \Gamma_{Ni} = 0$. However, the boundary between the bulk and surface regions is not a physical entity, and in principle, the surface region can have an arbitrary number of active layers. Consideration of a higher number of such layers should, in turn, yield improved accuracy of calculated surface properties such as surface energies and surface chemical potentials. Generalizing to arbitrary

active layers entails consideration of surface slabs with varying active layers for a fixed number of bulk layers. In this case, the rescaled excess Helmholtz free energy (f_s) is expressed independently in terms of the rescaled Pt surface excess (Γ_{Pt}) and the rescaled Ni surface excess (Γ_{Ni}); a zero rescaled surface excess of both species represents a surface with no active layers (**Equation 2**). We note that the generalized relationship is distinct from the case where a fixed number of active layers is considered, wherein Γ_{Pt} and Γ_{Ni} may not be independently varied (**Equation 1**). From **Equation 2**, a two dimensional convex hull is constructed with simplices in the form of planes that independently yield the chemical potentials of Pt (μ_{Pt}) and Ni (μ_{Ni}), as well as the surface energy (γ_s).

$$f_s = \gamma_s + \Gamma_{Pt}\mu_{Pt} + \Gamma_{Ni}\mu_{Ni} \quad (2)$$

Calculated surface chemical potentials of the alloy elements are compared with the corresponding bulk chemical potentials to identify surface structures and compositions that are in thermodynamic equilibrium with the bulk alloy. To evaluate the bulk chemical potentials of Pt (μ_{Pt}^{bulk}) and Ni (μ_{Ni}^{bulk}), a canonical bulk phase diagram with pure bulk Pt and pure bulk Ni as bulk references is constructed, and the slopes of the convex hull around Pt_3Ni are determined (see **Section S6**). The two slopes provide a lower bound ($\Delta\mu_{bulk}^{LB}$) and an upper bound ($\Delta\mu_{bulk}^{UB}$) on the surface chemical potentials, and any surface structures and compositions having surface chemical potential differences ($\Delta\mu = \mu_{Pt} - \mu_{Ni}$) within these bounds will be in equilibrium with the bulk alloy. We define these bounds as the bulk stability window.

$$\Delta\mu_{bulk}^{LB} \leq \Delta\mu \leq \Delta\mu_{bulk}^{UB} \quad (3)$$

We note that, since the canonical bulk phase diagram is calculated with pure bulk Pt and pure bulk Ni as references (different from the references of the surface chemical potentials), we apply a correction to the surface chemical potentials to align their references with the bulk references. We provide a derivation for the correction in **Section S6**.

3.3.2 Grand canonical ensemble

In the grand canonical analysis, the excess grand free energy of the surface (ω_s') is expressed as a function of the surface excess of Pt (Γ_{Pt}), the bulk composition of Pt (x_{Pt}), surface chemical potential

of Pt ($\bar{\mu}_{Pt}$), and excess Helmholtz free energy of the surface (f_s'), as shown in **Equation 4**. Note that, for convenience, the reference state for the chemical potentials is chosen to be the average energy per atom of bulk Pt_3Ni. This modified reference, compared to **Equations 1** and **2**, is indicated by the bar notation. In addition, for convenience, we use a stoichiometric $Pt_3Ni(111)$ surface as the reference for the grand canonical energies (indicated by the prime notation), in contrast to the canonical case described above (see **Section S4** for a more detailed derivation).

$$\omega_s' = f_s' - \frac{\Gamma_{Pt} - x_1}{1 - x_1}\bar{\mu}_{Pt} \tag{4}$$

To determine the chemical potentials, two equilibria are assumed—one between dissolved, solution-phase Ni ions and surface Ni atoms, and the other between bulk Pt atoms and surface Pt atoms. Therefore, the surface chemical potential of Ni is equated to the chemical potential of solution-phase Ni^{2+} ions, which is expressed as the sum of the standard chemical potential—the difference between the bulk DFT energy of Ni $\left(\mu_{Ni}^{bulk}\right)$ and standard free energy change of the redox reaction $\left(\Delta G^0_{Ni^{2+}|Ni}\right)$—and contributions from the solution-phase entropy, which depends on the concentration of Ni^{2+} ($C_{Ni^{2+}}$), and the electrode potential (U), referenced to the standard hydrogen electrode.

$$\mu_{Ni}^{sol} = \mu_{Ni}^{bulk} - \Delta G^0_{Ni^{2+}|Ni} + k_B T \log\frac{C_{Ni^{2+}}}{1M} - 2eU \tag{5}$$

The surface chemical potential of Pt is then determined using the bulk alloy constraint for the relationship between bulk Ni and Pt chemical potentials:

$$\bar{\mu}_{Ni} = \mu_{Ni}^{sol} - \mu_{Pt_3Ni}^{bulk} \tag{6}$$

$$\bar{\mu}_{Pt} = -\frac{(1 - x_1)\bar{\mu}_{Ni}}{x_1} \tag{7}$$

This formalism is analogous to a standard electrochemical Pourbaix analysis, wherein the grand free energy is expressed as a function of electrode potential. A surface Pourbaix diagram is made by plotting ω_s' against U (with the latter acting as a proxy for $\bar{\mu}_{Pt}$), and the most stable phase is determined at each potential by identifying the structure with lowest lying curve. Alloy structures with adsorbates,

specifically H, OH, and O, are included by modifying the expression for the excess grand free energy with an additional term incorporating the coverage (θ_{ads}) and chemical potential (μ_{ads}) of adsorbate species, the latter of which are estimated using the computational hydrogen electrode (CHE)[33] method. The factor N_l indicates the number of active layers.

$$\omega_s' = f_s' - \frac{\Gamma_{Pt} - x_1}{1 - x_1}\bar{\mu}_{Pt} - \frac{\theta_{ads}}{N_l}\mu_{ads} \quad (8)$$

4. Results and Discussion

4.1 Canonical surface phase analysis of the (111) facet

We begin with the discussion of the canonical surface phase diagram for the (111) facet (**Figure 1b**). The rescaled excess Helmholtz free energy (f_s) of each (111) configuration is plotted against the rescaled surface excess of Pt (Γ_{Pt}). Drawing an analogy between our canonical surface phase diagram and canonical bulk phase diagrams in literature, f_s can be interpreted as the energy required to form a Pt_3Ni surface alloy having a particular composition Γ_{Pt} from pure Ni and pure Pt surfaces, all of which have a Pt_3Ni bulk substrate. Extending this analogy further, the thermodynamic stability of surface phases can be determined using a convex hull formalism, wherein phases that lie on the convex hull are deemed to be thermodynamically stable, and those that do not lie on the hull are expected to separate out into the two adjacent phases on the hull. For each surface composition, we find that the surface structure with the lowest energy lies on the convex hull. We further confirm that this insight holds for larger unit cells by making the phase diagram and convex hull for a $\sqrt{3} \times \sqrt{3}$ cell with one active layer. We also consider stability at finite temperatures by evaluating f_s through a rigorous partition function-based approach at various temperatures (the convex hull for 1000 K, which is reported to be the annealing temperature in experimental studies[19], is shown in the phase diagram). At higher temperatures, all surface compositions are stabilized due to configurational entropy and remain on the convex hull. In aggregate, these results imply that no intrasurface phase transformations, such as islanding, will occur on $Pt_3Ni(111)$, although it is possible that such processes might be observed at larger length scales that are not accurately described by our surface unit cells.

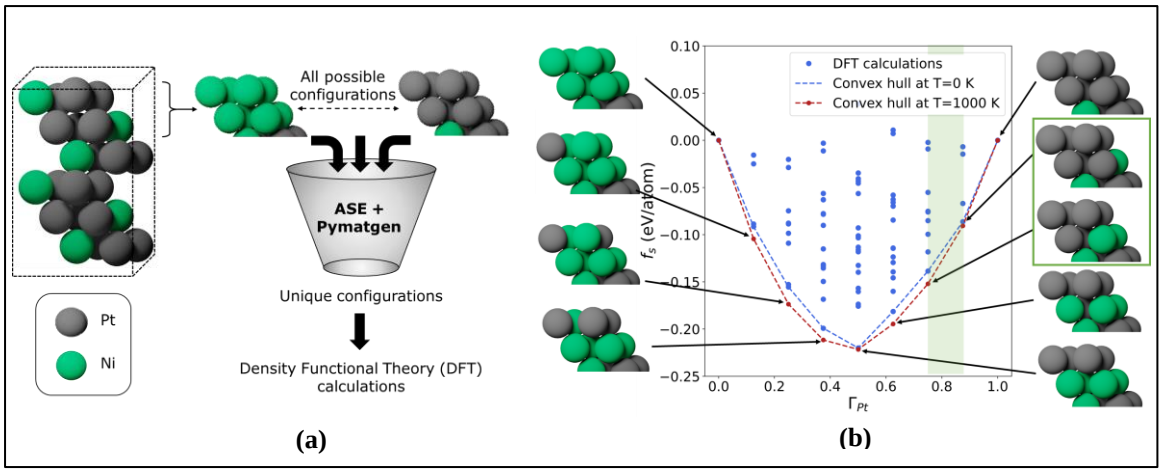

278

279 **Figure 1: (a)** Automated workflow to generate unique surface configurations from a stoichiometric
280 surface slab for any facet. First, all possible surface configurations are enumerated based on the number
281 of active layers specified (two, in this illustration). Next, an algorithm leveraging both ASE and
282 Pymatgen is used to identify unique, symmetrically-distinct configurations. These configurations are
283 then evaluated using DFT. **(b)** Canonical surface phase diagram showing the Helmholtz free energies
284 (per surface atom, f_s) plotted against the surface composition of Pt (Γ_{Pt}) (blue circles). The atoms in
285 the top two active layers of structures on the convex hull at T=0 K (blue dotted line) and T=1000 K (red
286 dotted line) are shown on the two sides of the phase diagram. The surface compositions lying in the
287 pale green window are in equilibrium with the bulk.

288 The results further demonstrate that, as the surface composition of Pt is increased, Pt preferentially
289 segregates into the top layer and forms a Pt skin at and above $\Gamma_{Pt} = 0.5$. This result is consistent with
290 prior surface science experiments and theoretical studies that have established the favorability of Pt
291 segregation to the (111) surface in stoichiometric Pt_3Ni alloys. We note that, compared to these prior
292 segregation analyses, we have additionally considered the stability of non-stoichiometric Pt surface
293 compositions, and we have determined that the segregation trends are consistent across all surface
294 compositions. The lowest surface excess free energy is at $\Gamma_{Pt} = 0.5$, corresponding to a structure with
295 a Pt skin and a fully Ni-occupied subsurface. In addition, this structure shows a higher fraction of mixed
296 Ni-Pt bonds compared to either Pt-Pt or Ni-Ni bonds in the active layers (see **Figure S6a**). This result
297 points to a strong driving force for formation of Pt-Ni bonds, in addition to Pt segregation. A theoretical
298 study by Abrikosov et al.[49] on $Pt_{0.5}Ni_{0.5}$ found two key governing principles that stabilize Pt-Ni alloy
299 surfaces—(1) the segregation of Pt to the top layer and (2) interlayer as well as intralayer Pt-Ni ordering.
300 Our results for the (111) facet, which clearly show both Pt segregation and maximization of the number
301 of Pt-Ni bonds, are consistent with these two principles. Finally, by comparing trends across Pt-based
302 alloys, we conclude that Pt-segregated structures are also stable on Pt_3Co, Pt_3Fe, and Pt_3Cu (see phase

diagrams in **Section S10**). As with $Pt_3Ni(111)$, intrasurface phase transformations are not observed on these alloys.

To further probe the stability of these surface structures under vacuum, we analyze the slopes of the canonical surface phase diagram that correspond to the difference in surface chemical potentials of Pt and Ni ($\Delta\mu$) (see **Section S6**). We apply the bulk stability constraint (discussed in **Methods** and **Section S6**), $0.11\ eV \leq \Delta\mu \leq 0.29\ eV$, to these surface chemical potentials to identify surface compositions that are in equilibrium with the bulk. We find (at both T=300 K and T=1000 K) that surface compositions in the range $\Gamma_{Pt} = 0.75 - 0.875$ (i.e., 75% to 87.5% Pt) are in equilibrium with the bulk (shown in green in **Figure 1b**). Our predictions are consistent with predictions made by Cao et al.[50] for equilibrium surface compositions (71% to 79%) and with the bulk chemical potential window (0.10 eV – 0.29 eV) predicted for Pt_3Ni by through a detailed cluster expansion-based Monte Carlo approach. The structures on the convex hull in this surface composition range have a Pt skin and approximately 50-75% Pt in the subsurface layer. Stamenkovic et al[7] report the formation of a Pt-skin and 48% Pt in the subsurface under UHV post-annealing. This experimentally reported segregation profile lies close to the range of segregation profiles predicted using DFT with our formalism.

The results described above demonstrate that it is possible to reliably predict the stable surface structure and composition of the $Pt_3Ni(111)$ surface under vacuum using only DFT calculations and thermodynamic consistency criteria. At the same time, use of larger unit cells or more active layers in the analyses could lead to higher resolution in the segregation profile.

4.2 Generalization of formalism to an arbitrary number of active layers

The treatments discussed above use a fixed number of active layers (in this case, two) where compositional changes are allowed to occur. This assumption implies that the surface excesses of the two species add to zero ($\Gamma_{Pt} + \Gamma_{Ni} = 0$); so species only substitute each other, and the total number of atoms in the active region is not changed. However, the choice of active region is somewhat arbitrary, and additionally, due to this restriction, it is not possible to calculate the surface chemical potentials of Pt and Ni and surface energies independently (we can only calculate the difference in chemical

potentials, as described in **Section 4.1**). To overcome these limitations, we briefly consider a generalization of our formalism by relaxing this constraint (so that $\Gamma_{Pt} + \Gamma_{Ni} \neq 0$) and analyzing a surface region with 0, 1, 2, and 3 active layers (corresponding to slabs having a total of 4, 5, 6, and 7 total layers, respectively). A full derivation of this generalized formalism is provided in **Section S2.** Briefly, we evaluate the excess Helmholtz energies (at 300 K) as well as surface excess concentrations of both species, for all generated structures and construct a three dimensional phase diagram. The *x*- and *y*-axes represent the rescaled surface excesses of Pt (Γ_{Pt}) and Ni (Γ_{Ni}), respectively, and the *z*-axis represents the rescaled excess Helmholtz energy (f_s) – see **Methods** section for exact definitions. A two dimensional projection of this phase diagram is shown in **Figure 2**, with the *z*-axis directed out of the page (for the full three dimensional representation, refer to **Figure S9f**). The thermodynamically stable structures are determined using a two dimensional convex hull whose simplices are planes.

The point ($\Gamma_{Pt} = 0, \Gamma_{Ni} = 0$) represents a surface with 0 active layers. For a constant Γ_{Ni}, an increase in Γ_{Pt} exclusively leads to an increase in the number of Pt atoms in the active surface region, and vice versa. Inclusion of each additional active layer then corresponds to the addition of a one dimensional convex hull having a slope of negative one and *y* (and *x*) intercepts equal to $\Gamma_{Pt} + \Gamma_{Ni}$ (the total excess for the given number of active layers). The primary advantage of this two dimensional convex hull formalism is that it allows us to calculate surface chemical potentials of Pt and Ni, as well as the surface energy, independently by determining the equation of each plane (or simplex) of the two dimensional convex hull. While, in principle, it is possible to add an arbitrarily large number of layers in this phase diagram, we find that the upper and lower bounds of the chemical potentials converge on adding three layers, and any further addition of layers only serves to increase the resolution of the phase diagram (see **Section S11**).

By equating surface chemical potentials with corresponding bulk values, we find a condition for the equilibrium of the surface with the bulk in terms of the surface excesses of Pt and Ni (the equilibrium region is shown in green in **Figure 2**). First, we observe that one of the vertices of the equilibrium region is at ($\Gamma_{Pt}^{(0)} = 0.34, \Gamma_{Ni}^{(0)} = 0$); for a zero surface excess of Ni, a positive surface excess of Pt is predicted in the equilibrium region. This result indicates that formation of a single layer Pt skin is

favored when it is equilibrated with the bulk, consistent with our result from the one dimensional analysis. Second, if we define $\frac{\Delta\Gamma_{Pt}}{\Delta\Gamma_{Ni}}$ as the slope of a line beginning at the vertex of the equilibrium region ($\Gamma_{Pt}^{(0)} = 0.34, \Gamma_{Ni}^{(0)} = 0$), then we observe that values of 1 and 3 bound the equilibrium region. This result implies the formation of a single layer Pt skin and subsurface compositions in the range of 50-75%, as observed in our DFT calculations. The analysis is also consistent with our prediction of the segregation profile using the one dimensional convex hull.

As mentioned above, the two dimensional treatment permits self-consistent calculation of relative surface energies and surface chemical potentials (**Figure S9**). The difference in surface chemical potentials is thus found to vary linearly with the logarithm of the ratio of the respective surface excesses, which is thermodynamically consistent with the mean-field expression of chemical potential as a logarithm of the activity (in this case, surface composition) (see **Figure S9e**). Although the existence of surface segregation implies that some non-mean field effects exist in the surface region, the logarithmic profile demonstrates that mean field factors nevertheless contribute significantly to the surface properties. Note these insights regarding the equilibrium surface composition profile are expected to change on the application of an external voltage, such as in an electrochemical environment, and this effect will be analyzed in a later section.

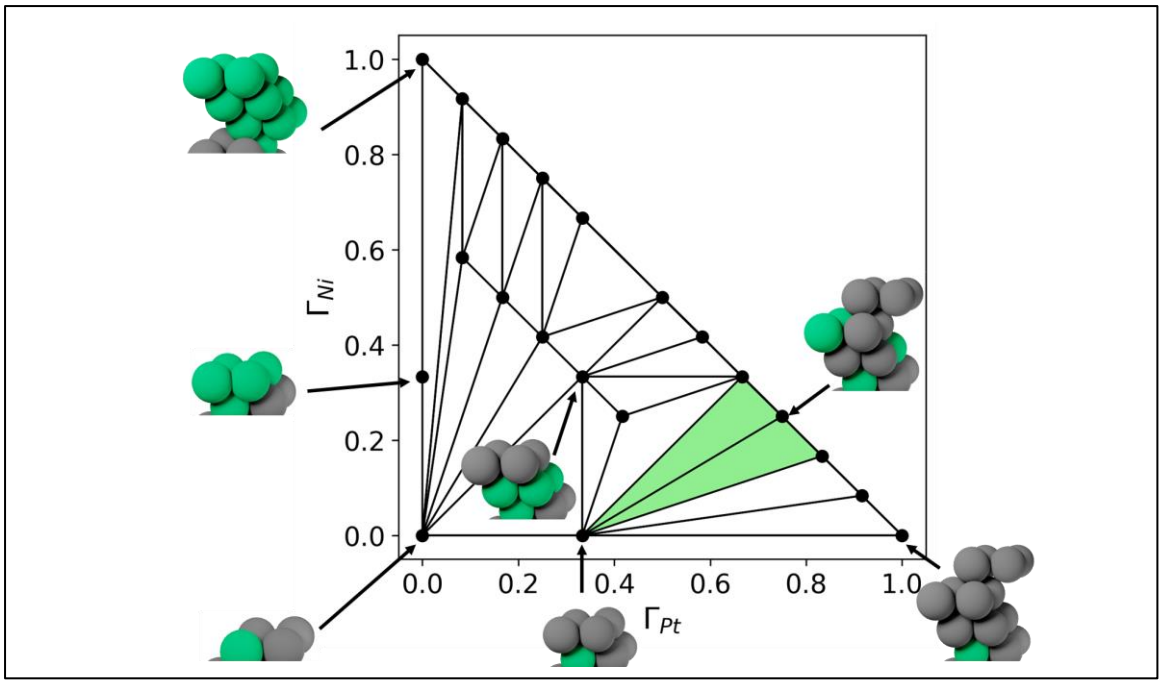

Figure 2: 2D projection of a 3D surface phase diagram with a 2D convex hull (represented by the triangles). A few selected structures on the convex hull are shown beside the phase diagram wherein Pt (grey) and Ni (green) atoms in the active layers are shown. The shaded green region on the convex hull represents the bulk-stable region.

4.3 Effect of surface coordination on segregation

To study the structure sensitivity of surface segregation profiles, we repeat the canonical analysis performed in **Section 4.1** for other surface facets such as (100), (110), and (211). We perform the analysis with the one dimensional convex hull formalism with two active layers, since we conclude from **Section 4.2** that the insights obtained using two active layers are consistent with those obtained by generalizing to an arbitrary number of active layers.

4.3.1 Segregation reversal on the (110) facet

On comparing segregation trends across facets, we find that none of the facets show a tendency for intrasurface phase separation. Moreover, the (100) facet shows a similar trend with regards to Pt skin formation as the (111) facet (see **Figure S7a** and **Table S4**). However, there is a complete reversal in the segregation trend for the (110) facet. On increasing the surface composition of Pt, Ni preferentially occupies the top layer, leading to the formation of a Ni skin above $\Gamma_{Pt} = 0.5$, as shown in **Figure 3a**. Gauthier et al.[51] report a reversal in the segregation trend and formation of a Ni skin for $Pt_{0.5}Ni_{0.5}$ (110). Moreover, Abrikosov et al.[49] report the same trend for $Pt_{0.5}Ni_{0.5}$ (110) using first principles DFT

calculations in the local density approximation (LDA) and attribute the reversal to a key difference in geometry of the (110) facet as compared to the (111) and (100) facets—the presence of an undercoordinated second layer (**Figure 3b**).

We examine the effect of Pt-Ni ordering on this reversal using a simple bond counting model. First, we estimate bulk "bond energies" of Pt-Pt, Pt-Ni, and Ni-Ni bonds, based on cohesive energies, as -0.49 eV/atom, -0.44 eV/atom, and -0.40 eV/atom, respectively. Second, we enumerate the number of surface bonds of each type in the top two layers for the Pt-segregated and Ni-segregated configurations at $\Gamma_{Pt} = 0.5$ for the (111) and (110) facets. We find that, for (111), two Pt-Ni bonds are replaced with one Pt-Pt and one Ni-Ni bond when comparing the Ni-segregated with the Pt-segregated surfaces, respectively. For (110), the opposite is true—three Pt-Pt bonds are replaced by two Pt-Ni bonds and one Ni-Ni bond when comparing the Ni-segregated with the Pt-segregated surfaces. Based on our evaluated bond energies, these bond numbers directly imply that the surface energy is minimized for Pt segregated (111) surfaces and for Ni segregated (110) surfaces. Note that, in this relatively simple model, we make an approximation by using bulk bond energy values to compare surface bonds; however, we do not expect the overall trend to change since the differences between bulk and surface bond energies are likely to be approximately equal for all bond pairs.

To determine whether the segregation reversal observed on the (110) facet extends to other surfaces with highly undercoordinated features, we further analyze the (211) facet of Pt_3Ni within our canonical formalism. We choose this surface because it possesses undercoordinated step sites (with a coordination number of seven) and because it serves as a general model of surface defects in many studies of heterogeneous catalysis and electrocatalysis.[52–54]

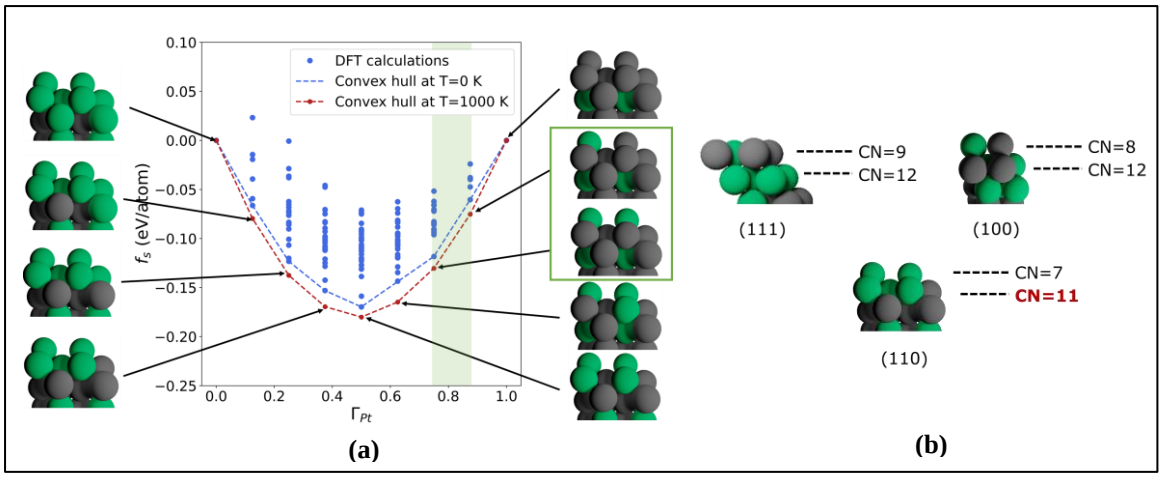

412

413 **Figure 3: (a)** Canonical surface phase diagram for the (110) facet showing the most stable structures at
414 every surface composition with the bulk stable region shaded in green. **(b)** The coordination numbers
415 of the top two layers in each of the (111), (100), and (110) facets. The (110) facet has an
416 undercoordinated second layer (marked in red).

417 ### 4.3.2 Segregation trends on the (211) facet

418 On applying our structure generation tools to the (211) facet, we discover that there are 4608 unique
419 configurations that can be generated by varying the positions of elements in the top two active layers.
420 This number is more than an order of magnitude higher than the total number of calculations for the
421 three low-index facets combined. The large size of the configuration space for the (211) facet can be
422 attributed to both its low symmetry and the large number of surface atoms per unit cell. To reduce the
423 associated computational cost, we introduce an active learning workflow that is briefly summarized
424 below.

425 We start with an initial dataset consisting of DFT-calculated excess Helmholtz energies for the (111),
426 (100), and (110) facets of Pt_3Ni, Pt_3Co, Pt_3Fe, and Pt_3Cu alloys (**Figure 4**). An additional 88
427 configurations of the (211) facet for each of the four alloys, generated by varying the surface structure
428 and composition of the top layer, are also calculated and added to the dataset, yielding a total of 1672
429 structures for all four alloys. A dropout graph convolutional network (dGCN)[45] is trained on this dataset
430 and used as a surrogate model to make predictions of excess Helmholtz energies for all unique
431 configurations of $Pt_3Ni(211)$ that can be generated by permuting the top two active layers (4608 in
432 total). A one dimensional convex hull is constructed based on the dGCN predictions, and a
433 thermodynamic criterion based on a lower confidence bound (LCB) acquisition function is used to

sample structures near the convex hull for evaluation using DFT. The dGCN is then retrained on the updated dataset, and the procedure is repeated until no new configurations are predicted to lie on the convex hull. Based on the converged results, a canonical surface phase diagram is plotted with the DFT-evaluated excess Helmholtz energies of the most stable $Pt_3Ni(211)$ structures (**Figure 5a**). A detailed description of this workflow is provided in **Section S7.**

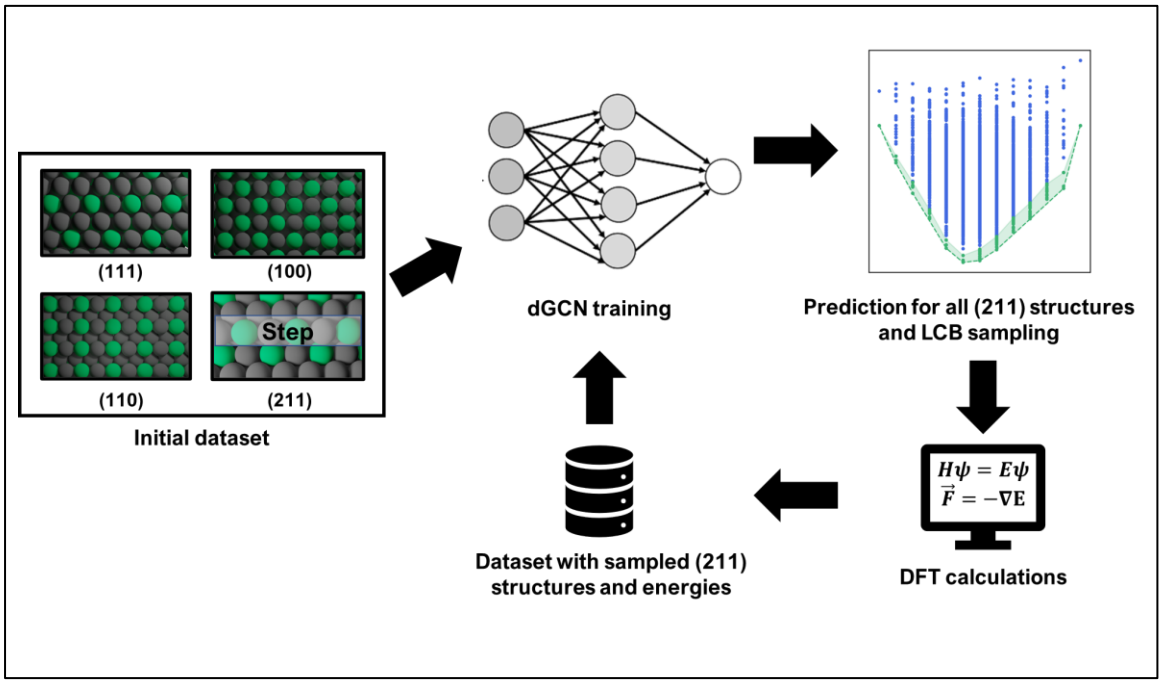

Figure 4: Active learning workflow to identify stable configurations of irregular facets. A training dataset consisting primarily of regular facets (and a relatively small subset of irregular facets) is generated using DFT calculations. The dGCN is trained on this initial dataset. Subsequently, predictions are made for all (211) configurations using the dGCN and a canonical surface phase diagram is constructed. Based on a lower confidence bound acquisition function, a few stable configurations are chosen, DFT energies are evaluated for them, and these are added to the training set. The dGCN is retrained on this new training dataset to improve predictions. This cyclic workflow is repeated until no new structures are added predicted to lie on the convex hull.

The canonical phase diagram predicts the formation of a Pt skin as the surface composition of Pt is increased (**Figure 5a**). The surface structure in equilibrium with the bulk is found to have a Pt skin and 50% Ni in the second layer, with two out of the three subsurface Ni atoms situated directly below the stepped edge and the remaining Ni atom present below the upper terrace. In addition, the presence of Pt atoms in the top layer is found to be governed by surface coordination. Pt atoms first occupy the lower terrace, which has a coordination number of 10, following which the upper terrace, with a coordination number of 9, becomes occupied as Γ_{Pt} increases. Finally, at $\Gamma_{Pt} = 0.5$, Pt atoms occupy

the two sites on the step edge that have a coordination number of 7 (**Figure 5b**). Thus, the propensity for Pt segregation to a surface site is directly proportional to the coordination number of the site. To provide further insight into these trends, we calculate cohesive energies, using the bulk bond strengths described above, for Pt and Ni atoms on both the lower terrace and the step in a stoichiometric Pt_3Ni slab. The difference between the magnitude of the total cohesive energy, for all bonds, on the lower terrace and on the step is 1.45 eV/atom for Pt and 0.51 eV/atom for Ni, indicating a Pt atom is approximately thrice as stable on the lower terrace, as compared to the step site, than a Ni atom.

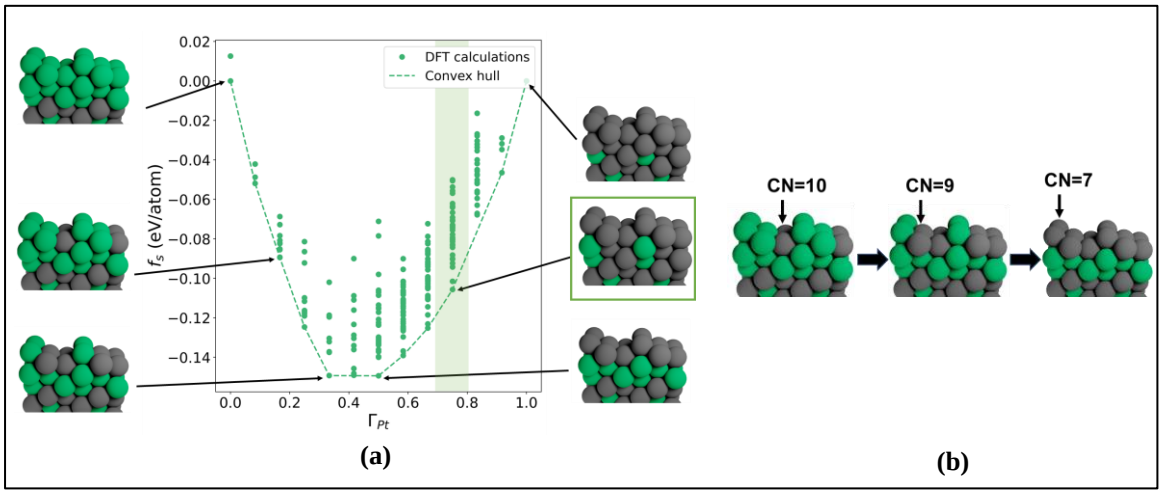

Figure 5: (a) Canonical surface phase diagram of Pt_3Ni (211) from DFT-predicted excess Helmholtz free energies of configurations sampled using the active learning workflow. The shaded region represents compositions that are in equilibrium with the bulk, and the structure with the green box represents a bulk-stable structure. (211) slabs shown here are repeated once in the *x*-direction for clarity. **(b)** Occupation of surface with increasing surface excess composition of Pt is in decreasing order of surface coordination.

To summarize, for the (110) facet, a higher surface composition is required to form a Pt skin, which falls outside the equilibrium region, and thus, a reversal in segregation is seen. For (211), the surface composition required to form a Pt skin is lower than the equilibrium region, so a Pt skin is predicted to be stable. These results suggest that local surface structure and coordination of a facet plays an important role in regulating the presence (or absence) of a Pt skin.

4.4 Electrochemical surface stability analyses

In an electrochemical environment (such as in a fuel cell), the solution-phase chemical potentials of Pt and Ni can additionally influence the surface structure and composition in this analysis. For instance, a

lower solution-phase chemical potential of an element can lead to leaching of that element from the surface into the solution. Further, water-derived adsorbates present in an aqueous electrolyte may interact with the surface and form surface hydroxide or oxide phases. These effects may be convoluted and also depend on the electrode potential. Having performed a detailed stability analysis under vacuum, we turn to the analysis of electrochemical stability.

4.4.1 Comparison of bulk, surface, and solution-phase chemical potentials

We begin with a simple comparison of bulk, surface, and solution phase chemical potentials of Pt and Ni. Bulk chemical potentials are obtained from a bulk phase diagram analysis (**Section S6**)**.** Surface chemical potentials are, in turn, obtained from the two dimensional convex hull analysis (**Section 4.2**). The Nernst is equation is used to calculate solution phase chemical potentials by assuming the presence of $10^{-6}\ M$ of Pt^{2+} and Ni^{2+} ions at 300 K in the electrolyte. The reference state for the chemical potentials of all phases for each element is taken to be the chemical potential of a pure bulk structure of that element (for instance, pure bulk Pt is the reference for bulk, surface, and solution-phase Pt chemical potentials).

The comparison between these chemical potentials is summarized in a chemical potential diagram (akin to a reaction free energy diagram) in **Figure 6**. First, we observe that for both Pt and Ni, the bulk and surface chemical potentials for equal bulk (x) and surface (Γ) compositions (for example, $x_{Ni} = \Gamma_{Ni} = 0.25$) are nearly equal, indicating that there is no chemical potential gradient and hence, no net transfer of Pt and Ni between the bulk and surface when they both have the same composition. This result provides rigorous support for the common assumption that, in the absence of large diffusion barriers, the bulk and surface regions of binary alloys are in thermodynamic equilibrium.

Second, on exposing a Pt_3Ni alloy nanoparticle to an electrolyte in a fuel cell, the application of a voltage leads to significant changes in chemical potentials, thus introducing driving forces for changes in the bulk, surface, and solution phase concentrations of Pt and Ni. For Ni, at both $U = 0.9\ V_{SHE}$ and $U = 1.2\ V_{SHE}$ (ORR relevant voltages), the solution phase chemical potential is significantly lower than the bulk and surface chemical potentials. Therefore, there is a driving force for diffusion of Ni from the bulk to the surface (lowering the bulk chemical potential) and leaching from the surface into the solution

(lowering the surface chemical potential) which, in turn, would lead to an increase in the solution phase concentration of Ni^{2+} and a corresponding increase in the solution-phase chemical potential of Ni. Overall, this implies a net transfer of Ni from the bulk to the solution. For Pt, at $U = 0.9\,V_{SHE}$, the approach to equilibrium is reversed—there is a driving force for the redeposition of Pt^{2+} ions onto the surface (lowering the solution phase chemical potential) and diffusion of Pt from the surface to the bulk (lowering the surface chemical potential), leading to a corresponding increase in the bulk chemical potential of Pt. In effect, this signifies a net transfer of Pt from the solution to the bulk. However, if there is an increase in the potential to $U = 1.2\,V_{SHE}$, due to potential cycling or fuel cell startup or shutdown, the driving forces resemble that of Ni, and leaching of Pt begins to be favored.

While we have painted a picture of thermodynamic equilibrium above, it is possible for kinetic limitations, such as hindered diffusion, to prevent approach to equilibrium. In fact, it is found in experiments that Pt skin formation in an electrochemical environment terminates at a certain number of layers[6,19,55]. In such a case, it is possible for the surface to be kinetically trapped, implying that, in our diagram, the surface chemical potential would take an intermediate value between the bulk and solution phase chemical potentials. Additionally, it is possible for adsorbates present in the electrolyte to bind to the surface and modify the surface chemical potential through processes such as surface oxidation. To analyze these scenarios, we next turn to the grand canonical analysis.

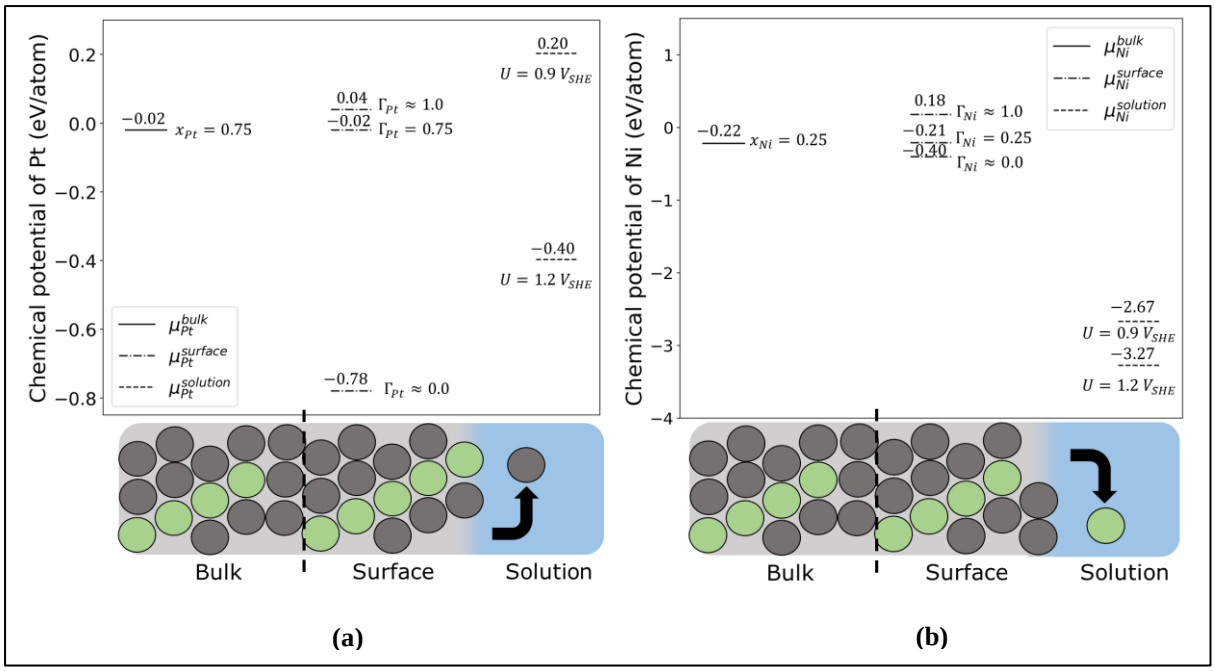

Figure 6: Chemical potential diagrams for **(a)** Pt and **(b)** Ni. Bulk, surface, and solution phase states are shown as solid, dash-dot, and dashed lines, respectively, and the values above these states represent corresponding chemical potentials in units of eV/atom. For solution phase states, corresponding voltages are specified below the states.

4.4.2 Grand canonical analysis

To study the influence of water-derived adsorbates on the structures of Pt_3Ni surfaces in electrochemical environments, we adopt a grand canonical approach. In this formalism, the excess grand free energy (ω_s') is calculated as a function of the chemical potential of each species in the structure. By adopting appropriate quasi-equilibrium assumptions, it is possible to express the chemical potential of each species as a function of the electrode potential via the Nernst equation for Ni, bulk alloy constraint for Pt, and the computational hydrogen electrode (CHE)[33] method for H, OH, and O adsorbates, rendering the excess grand free energy as a sole function of the electrode potential.

The results are presented in the form of a surface Pourbaix diagram (at pH=0) in **Figure 7**. We note that this approach has been utilized by Hansen et al.[56] to find stable phases on metal surfaces under electrochemical conditions. Further, Nørskov and coworkers[57] have introduced an active learning-based automated approach to constructing these surface Pourbaix diagrams with varying adsorbate coverages. Herein, we expand on these approaches by constructing surface Pourbaix diagrams for alloy surfaces with varying surface facets, structures, and compositions.

Below, we provide a detailed analysis of the structure and stability of two Pt_3Ni facets—the close-packed (111) facet and the stepped (211) facet - since these well represent terraces and edges in a cuboctahedral nanoparticle; results for the other facets are discussed in **Section S12**. We begin by discussing the surface Pourbaix diagram for the (111) facet (**Figure 7a**), and we then compare trends with the (211) facet (**Figure 7b**). For each facet, we consider all structures on the convex hulls in the corresponding canonical analyses (**Figures 1**, **3**, **5**, and **S10a**). In addition, since surface adsorption can, in some cases, lead to reversal of surface segregation, we consider structures wherein the first two layers of each convex hull structure are interchanged (the most stable arrangement of atoms in each layer for the interchanged structures is chosen for analysis). The excess grand free energy of each structure is plotted against the electrode potential, and each line represents a clean surface structure of Pt_3Ni. The influence of three adsorbates—H, OH, and O—is additionally analyzed, and structures covered by these adsorbates are represented in the form of grey, blue, and red envelopes, respectively. On the (111) facet, we consider coverages of 1/4 ML for each adsorbate, while coverages of 1/6 ML are employed for the (211) facet. The energy of the most favorable site for each adsorbate is used to generate the Pourbaix diagrams (for OH, a solvation correction is added for top site adsorption - see **Section S4.1**).

On the (111) facet, at potentials lower than about -0.75 V_{SHE}, the most stable structure has a pure Ni surface with ¼ ML H. On increasing the potential, Pt atoms occupy the top layer until a single layer Pt skin is formed, following which they occupy the subsurface until a multilayer Pt skin is formed above -0.22 V_{SHE}. This transformation can be attributed to the segregation and subsequent leaching of Ni from the surface. We note that an alternate process — adsorbate-induced segregation of Ni, followed by surface oxidation – can, in principle, also influence the surface structures. However, since the lower boundaries of both the blue and red envelopes, representing structures with OH and O adsorbates, respectively, are higher in free energy than other structures at any potential where Ni is present in the top two layers, such oxygen-induced segregation processes are not thermodynamically preferred. Effectively, in an electrochemical environment, Ni atoms preferentially leach into solution, and adsorbed O or OH moieties do not form. As the potential is increased above 0.2 V_{SHE}, the surface

transitions from a hydrogen-covered surface to a clean surface. Finally, as the potential is increased above 0.85 V_{SHE}, the adsorption of OH and, subsequently, O on the multilayer Pt skin becomes favorable, indicating that surface oxidation is the dominating surface-altering mechanism above that potential. These results are broadly consistent with the work of Stamenkovic et al., who report the formation of a "Pt skeleton," composed of a Pt-rich surface with bulk-structured layers in the subsurface region, after electrochemical cycling between 0.05 V_{SHE} and 1.0 V_{SHE}. According to our surface Pourbaix analysis, above 0 V_{SHE}, multilayer Pt skins with a bulk terminated subsurface (rather than a Ni-enriched subsurface) are predicted to be stable, qualitatively matching the aforementioned experimental results.

The (211) stepped facet shows similar trends compared to the (111) facet. However, since step sites bind adsorbates strongly as compared to terrace sites on (111), the clean surface of the (211) facet is not stable in any potential region, with the transition from H to OH adsorbates occurring at 0.5 V_{SHE} and the transition from OH to O occurring at 0.85 V_{SHE}. Additionally, the excess grand free energy difference between the clean surface and the OH and O envelopes is lower for all potentials compared to (111), indicating that metastable surface hydroxylation or oxidation are more likely to occur on (211). We note, in passing, that these transition potentials may be modified on consideration of higher coverages on both (111) and (211), but we do not expect the general trends to change.

The Pourbaix analysis also implies that multilayer Pt skins are metastable at potentials relevant to the ORR. By representing the bulk stability window in terms of electrode potential, we find that that bulk Pt_3Ni is stable between -0.33 V_{SHE} and -0.27 V_{SHE}. Above -0.27 V_{SHE}, it is favorable for Ni to leach from the bulk. Thus, under ORR conditions, the surface Pourbaix analysis will predict the complete conversion of all Pt_3Ni layers to Pt if more active layers are included in the calculations. However, since it is observed experimentally that this multilayer skin formation stops at a finite number of layers[6,19,55], it can be concluded that the resultant structures are kinetically trapped.

In closing, we remark that the approach presented above may be particularly useful in predicting the stable surface phases of multimetallic or "high-entropy" alloys under reaction conditions, since the presence of several elements with differing dissolution and oxidation potentials can lead to the

formation of mixed stable phases with the possibility of simultaneous segregation, leaching, and surface oxidation. Additionally, while the effect of excess configurational entropy in stabilizing the surface is negligible in this case (see **Figure S11**), for a high-entropy alloy with more than five elements, this effect may lead to a more pronounced shift in surface dissolution and oxidation potentials.

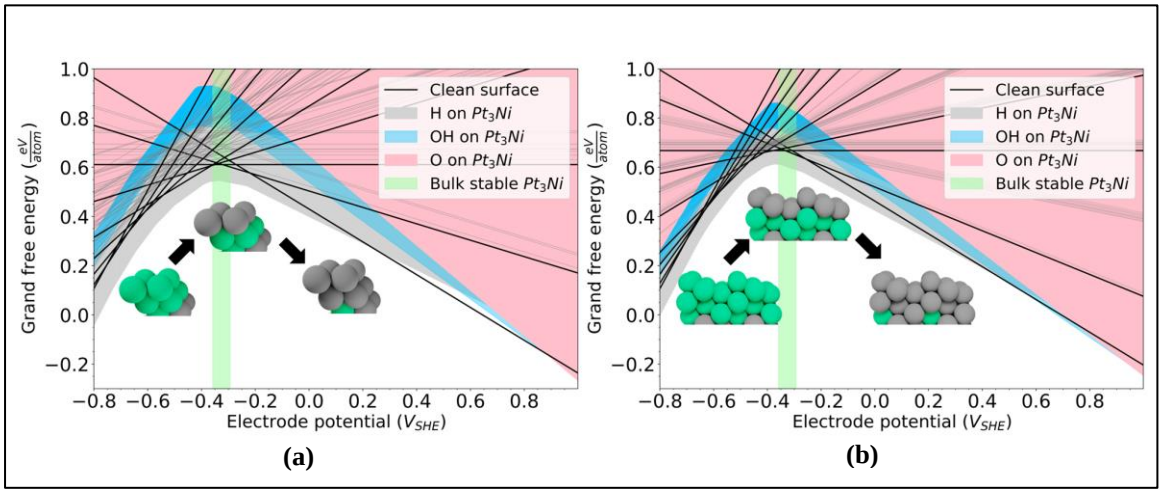

Figure 7: Surface Pourbaix diagram of the **(a)** (111) facet and **(b)** (211) facet. Black solid lines represent surface configurations that are stable at some potential. Grey solid lines represent configurations that are not stable at any potential. Grey, pink, and blue envelopes represent the most stable H-, O- and OH-adsorbed configurations, respectively. The shaded green region represents the potential range in which bulk Pt_3Ni is stable. The evolution of the surface with change in potential is illustrated with a few key structures in both diagrams.

5. Conclusions

We develop and present a computational framework to perform a rigorous study of surface stability of alloy catalysts. Our work generalizes previous first principles studies on surface stability by accounting for all possible surface structures and compositions (for a given unit cell), different facets, and diverse chemical environments. Additionally, our formalism allows for the study of combined influence of multiple mechanisms such as segregation, leaching, intrasurface phase transformations, and surface oxidation, which can affect the surface in an electrochemical environment. The atomistic model utilized in the framework consists of two regions, a fixed bulk region and a surface region with a fixed number of active layers in which all the structural and compositional perturbations are sampled. Pt_3Ni, which is a state-of-the-art alloy catalyst for ORR, is used as a model system to demonstrate the key features of this framework.

First, a canonical surface phase diagram is plotted for $Pt_3Ni(111)$ based on the rescaled excess Helmholtz energies of all the sampled structures evaluated using DFT. A one dimensional convex hull is used to determine stable structures at all given surface compositions. The phase diagram predicts the favorability of Pt segregation to the surface under vacuum, and it also identifies a single layer Pt skin structure, with 50-75% Ni in the second layer, that is in equilibrium with the bulk. This result, which is consistent with prior experiments and computational studies, is then generalized to an arbitrary number of active layers using a 2-dimensional convex hull analysis, and surface chemical potentials and surface energies are calculated self-consistently as a function of the surface composition. The relationship between the difference in surface chemical potentials and the logarithm of the ratio of surface excess concentrations is found to be well represented by a linear fit, analogous to the mean-field expression of chemical potential as a function of activity.

Second, on repeating the canonical analysis for the (110) facet, we find that the formation of a Ni skin is favored, in stark contrast to the (111) facet. A simple bond counting model is developed to explain the differences in segregation trends between the (111) and (110) facets. Further, to ascertain whether inverse segregation is favored on other surface facets, we examine segregation trends on a highly stepped $Pt_3Ni(211)$ surface. Since we find that the search space of structures for the (211) facet is about an order of magnitude higher than the regular facets, we use a dropout graph convolutional network (dGCN) in conjunction with a thermodynamics-based acquisition function to reduce the number of DFT evaluations required from 4608 to 1892 for Pt_3Ni, with a further reduction expected on application of this workflow to other alloys in the dataset. From the phase diagram of $Pt_3Ni(211)$, we find that, as the surface composition of Pt is increased, Pt segregates to the lower terrace (coordination number of 10), followed by the upper terrace (coordination number of 9), and finally to the step edge (coordination number of 7) in the top layer. This result signifies that surface segregation of Pt is dependent on the coordination environment of a surface facet.

Finally, we analyze the electrochemical stability of Pt_3Ni. We first perform a simple comparison of the bulk, surface, and solution phase chemical potentials, the former two calculated from the canonical analyses, and the latter calculated using the Nernst equation, and discuss implications of these chemical

potentials for Pt and Ni dissolution as the system approaches equilibrium. We then shift to the grand canonical ensemble in which the excess grand free energy is expressed as a function of the electrode potential. As the potential is increased, the surface composition of Pt_3Ni (111) is found to change from Ni-rich to Pt-rich, with multilayer Pt skins stable above $0\ V_{SHE}$ due to segregation and subsequent leaching of Ni from the surface. However, since the bulk dissolution potential of Ni is determined to be $-0.27\ V_{SHE}$, the multilayer Pt skins are likely to be only kinetically stable under realistic ORR conditions. This result is consistent with experimental reports that indicate formation of multilayer Pt skins on potential cycling between $0.05\ V_{SHE}$ and $1\ V_{SHE}$. We also conclude that, for the (111) surface, leaching dominates over surface hydroxylation and surface oxidation at lower potentials, with the surface hydroxylation onset only occurring at $0.85\ V_{SHE}$. For (211), this onset occurs at a much lower potential ($0.5\ V_{SHE}$), and there is a greater driving force for metastable surface hydroxylation or oxidation. We envision that these surface phase analyses could be used to rigorously quantify the stability of, not only bimetallic alloys, but also multimetallic, high-entropy alloys under electrochemical conditions.

6. Acknowledgements

The authors acknowledge the United States Department of Energy through the Office of Science, Office of Basic Energy Sciences (BES), Chemical, Biological, and Geosciences Division, Data Science Initiative, grant DE-SC0020381. Use of the Center for Nanoscale Materials, U.S. Department of Energy, Office of Science, Office of Basic Energy Sciences User Facility under Contract No. DE-AC02-06CH11357, and of the computational resources from the Nation Energy Research Scientific Computing Center, is also acknowledged.

7. Competing Interests

The Authors declare no Competing Financial or Non-Financial Interests.

8. Author Contributions

G. D. performed Density Functional Theory calculations, analyzed the data, designed the active learning workflow, contributed to the development of the formalism, and co-wrote the manuscript. P. G. contributed to the active learning workflow design and co-wrote the manuscript. J.G. supervised research, contributed to the development of the formalism, and co-wrote the manuscript.

9. Data Availability

Upon acceptance, the raw data sets of alloy structures and scripts/notebooks used to perform the analysis with them will uploaded to the following GitHub repository: https://github.itap.purdue.edu/GreeleyGroup/alloy_stability

10.References

(1) Greeley, J.; Mavrikakis, M. Alloy Catalysts Designed from First Principles. *Nat. Mater.* **2004**, *3* (11), 810–815. https://doi.org/10.1038/nmat1223.

(2) Greeley, J.; Stephens, I. E. L.; Bondarenko, A. S.; Johansson, T. P.; Hansen, H. A.; Jaramillo, T. F.; Rossmeisl, J.; Chorkendorff, I.; Nørskov, J. K. Alloys of Platinum and Early Transition Metals as Oxygen Reduction Electrocatalysts. *Nat. Chem.* **2009**, *1* (7), 552–556. https://doi.org/10.1038/nchem.367.

(3) Hansen, H. A.; Shi, C.; Lausche, A. C.; Peterson, A. A.; Nørskov, J. K. Bifunctional Alloys for the Electroreduction of CO2 and CO. *Phys. Chem. Chem. Phys.* **2016**, *18* (13), 9194–9201. https://doi.org/10.1039/c5cp07717f.

(4) Gasteiger, H. A.; Markovic, N.; Ross, P. N.; Cairns, E. J. Well-Characterized Pt-Ru Alloys Diffraction _ _ Pt. **1993**, 12020–12029.

(5) Gurau, B.; Viswanathan, R.; Liu, R.; Lafrenz, T. J.; Ley, K. L.; Smotkin, E. S.; Reddington, E.; Sapienza, A.; Chan, B. C.; Mallouk, T. E.; Sarangapani, S. Structural and Electrochemical

690 Characterization of Binary, Ternary, and Quaternary Platinum Alloy Catalysts for Methanol
691 Electro-Oxidation. *J. Phys. Chem. B* **1998**, *102* (49), 9997–10003.
692 https://doi.org/10.1021/jp982887f.

693 (6) Stamenkovic, V. R.; Mun, B. S.; Arenz, M.; Mayrhofer, K. J. J.; Lucas, C. A.; Wang, G.; Ross,
694 P. N.; Markovic, N. M. Trends in Electrocatalysis on Extended and Nanoscale Pt-Bimetallic
695 Alloy Surfaces. *Nat. Mater.* **2007**, *6* (3), 241–247. https://doi.org/10.1038/nmat1840.

696 (7) Stamenkovic, V. R.; Fowler, B.; Mun, B. S.; Wang, G.; Ross, P. N.; Lucas, C. A.; Markovic, N.
697 M. Improved Oxygen Reduction Activity on Pt3Ni(111) via Increased Surface Site Availability.
698 *Science (80-.).* **2007**, *315* (5811), 493–497. https://doi.org/10.1126/science.1135941.

699 (8) Wu, J.; Zhang, J.; Peng, Z.; Yang, S.; Wagner, F. T.; Yang, H. Truncated Octahedral Pt3Ni
700 Oxygen Reduction Reaction Electrocatalysts. *J. Am. Chem. Soc.* **2010**, *132* (14), 4984–4985.
701 https://doi.org/10.1021/ja100571h.

702 (9) Tian, X.; Zhao, X.; Su, Y.-Q.; Wang, L.; Wang, H.; Dang, D.; Chi, B.; Liu, H.; Hensen, E. J.
703 M.; Xiong, W.; Lou, D.; Xia, B. Y. *Engineering Bunched Pt-Ni Alloy Nanocages for Efficient*
704 *Oxygen Reduction in Practical Fuel Cells*.

705 (10) Chen, C.; Kang, Y.; Huo, Z.; Zhu, Z.; Huang, W.; Xin, H. L.; Snyder, J. D.; Li, D.; Herron, J.
706 A.; Mavrikakis, M. Highly Crystalline Multimetallic Nanoframes with Three-Dimensional
707 Electrocatalytic Surfaces. *Science (80-.).* **2014**, *343* (6177), 1336–1339.
708 https://doi.org/10.1126/science.1246310.

709 (11) Wang, C.; Markovic, N. M.; Stamenkovic, V. R. Advanced Platinum Alloy Electrocatalysts for
710 the Oxygen Reduction Reaction. *ACS Catal.* **2012**, *2* (5), 891–898.
711 https://doi.org/10.1021/cs3000792.

712 (12) Colón-Mercado, H. R.; Popov, B. N. Stability of Platinum Based Alloy Cathode Catalysts in
713 PEM Fuel Cells. *J. Power Sources* **2006**, *155* (2), 253–263.
714 https://doi.org/10.1016/J.JPOWSOUR.2005.05.011.

(13) Ma, Y.; Balbuena, P. B. Pt Surface Segregation in Bimetallic Pt3M Alloys: A Density Functional Theory Study. *Surf. Sci.* **2008**, *602* (1), 107–113. https://doi.org/10.1016/j.susc.2007.09.052.

(14) Ruban, A. V.; Skriver, H. L.; Nørskov, J. K. Surface Segregation Energies in Transition-Metal Alloys. *Phys. Rev. B - Condens. Matter Mater. Phys.* **1999**, *59* (24), 15990–16000. https://doi.org/10.1103/PhysRevB.59.15990.

(15) McCue, I.; Benn, E.; Gaskey, B.; Erlebacher, J. Dealloying and Dealloyed Materials. *https://doi.org/10.1146/annurev-matsci-070115-031739* **2016**, *46*, 263–286. https://doi.org/10.1146/ANNUREV-MATSCI-070115-031739.

(16) Callejas-Tovar, R.; Diaz, C. A.; De La Hoz, J. M. M.; Balbuena, P. B. Dealloying of Platinum-Based Alloy Catalysts: Kinetic Monte Carlo Simulations. *Electrochim. Acta* **2013**, *101*, 326–333. https://doi.org/10.1016/J.ELECTACTA.2013.01.053.

(17) Greeley, J.; Nørskov, J. K. Electrochemical Dissolution of Surface Alloys in Acids: Thermodynamic Trends from First-Principles Calculations. *Electrochim. Acta* **2007**, *52* (19), 5829–5836. https://doi.org/10.1016/j.electacta.2007.02.082.

(18) Ma, Y.; Balbuena, P. B. Surface Properties and Dissolution Trends of Pt3M Alloys in the Presence of Adsorbates. *J. Phys. Chem. C* **2008**, *112* (37), 14520–14528. https://doi.org/10.1021/jp8046888.

(19) Stamenkovic, V. R.; Mun, B. S.; Mayrhofer, K. J. J.; Ross, P. N.; Markovic, N. M. Effect of Surface Composition on Electronic Structure, Stability, and Electrocatalytic Properties of Pt-Transition Metal Alloys: Pt-Skin versus Pt-Skeleton Surfaces. *J. Am. Chem. Soc.* **2006**, *128* (27), 8813–8819. https://doi.org/10.1021/ja0600476.

(20) Politano, A.; Caputo, M.; Goldoni, A.; Torelli, P.; Chiarello, G. Segregation and Selective Oxidation of Ni Atoms in Pt3Ni(111) in a Low-Pressure Oxygen Environment. *J. Phys. Chem. C* **2013**, *117* (51), 27007–27011. https://doi.org/10.1021/jp409917b.

(21) Sun, D.; Zhao, Y.; Su, H.; Li, W. An Atomistic Thermodynamics Study of the Structural

Evolution of the Pt3Ni(111) Surface in an Oxygen Environment. *Cuihua Xuebao/Chinese J. Catal.* **2013**, *34* (7), 1434–1442. https://doi.org/10.1016/s1872-2067(12)60604-4.

(22) Greeley, J.; Nørskov, J. K. Combinatorial Density Functional Theory-Based Screening of Surface Alloys for the Oxygen Reduction Reaction. *J. Phys. Chem. C* **2009**, *113* (12), 4932–4939. https://doi.org/10.1021/jp808945y.

(23) Christensen, A.; Ruban, A. V; Stoltze, P.; Jacobsen, K. W.; Skriver, H. L.; No, J. K.; Besenbacher, F. Phase Diagrams for Surface Alloys. **1997**.

(24) Ma, Y.; Balbuena, P. B. Surface Segregation in Bimetallic Pt3M (M = Fe, Co, Ni) Alloys with Adsorbed Oxygen. *Surf. Sci.* **2009**, *603* (2), 349–353. https://doi.org/10.1016/j.susc.2008.11.036.

(25) Reuter, K.; Scheffler, M. First-Principles Atomistic Thermodynamics for Oxidation Catalysis: Surface Phase Diagrams and Catalytically Interesting Regions. **2003**, *90* (4). https://doi.org/10.1103/PhysRevLett.90.046103.

(26) Kitchin, J. R.; Reuter, K.; Scheffler, M. Alloy Surface Segregation in Reactive Environments: First-Principles Atomistic Thermodynamics Study of Ag3 Pd(111) in Oxygen Atmospheres. *Phys. Rev. B - Condens. Matter Mater. Phys.* **2008**, *77* (7), 1–12. https://doi.org/10.1103/PhysRevB.77.075437.

(27) Kim, J.; Hyeon Park, W.; Doh, W. H.; Lee, S. W.; Noh, M. C.; Gallet, J.-J.; Bournel, F.; Kondoh, H.; Mase, K.; Jung, Y.; Mun, S.; Park, J. Y. *Adsorbate-Driven Reactive Interfacial Pt-NiO 1−x Nanostructure Formation on the Pt 3 Ni(111) Alloy Surface*; 2018.

(28) Bao, H.; Li, J.; Jiang, L.; Shang, M.; Zhang, S.; Jiang, Z.; Wei, X.; Huang, Y.; Sun, G.; Wang, J.-Q. Structure of Pt n Ni Nanoparticles Electrocatalysts Investigated by X-Ray Absorption Spectroscopy. **2013**. https://doi.org/10.1021/jp404799d.

(29) Cao, L.; Niu, L.; Mueller, T. Computationally Generated Maps of Surface Structures and Catalytic Activities for Alloy Phase Diagrams. **2019**, *116* (44), 22044–22051.

https://doi.org/10.1073/pnas.1910724116.

(30) Cao, L.; Mueller, T. Rational Design of Pt3Ni Surface Structures for the Oxygen Reduction Reaction. *J. Phys. Chem. C* **2015**, *119* (31), 17735–17747. https://doi.org/10.1021/acs.jpcc.5b04951.

(31) Han, S.; Lysgaard, S.; Vegge, T.; Hansen, H. A. Rapid Mapping of Alloy Surface Phase Diagrams via Bayesian Evolutionary Multitasking. *npj Comput. Mater.* **2023**, *9* (1). https://doi.org/10.1038/s41524-023-01087-4.

(32) Han, S.; Barcaro, G.; Fortunelli, A.; Lysgaard, S.; Vegge, T.; Hansen, H. A. Unfolding the Structural Stability of Nanoalloys via Symmetry-Constrained Genetic Algorithm and Neural Network Potential. *npj Comput. Mater.* **2022**, *8* (1), 1–11. https://doi.org/10.1038/s41524-022-00807-6.

(33) Nørskov, J. K.; Rossmeisl, J.; Logadottir, A.; Lindqvist, L.; Kitchin, J. R.; Bligaard, T.; Jónsson, H. Origin of the Overpotential for Oxygen Reduction at a Fuel-Cell Cathode. *J. Phys. Chem. B* **2004**, *108* (46), 17886–17892. https://doi.org/10.1021/jp047349j.

(34) Gal, Y.; Uk, Z. A. *Dropout as a Bayesian Approximation: Representing Model Uncertainty in Deep Learning Zoubin Ghahramani*; 2016.

(35) Deshmukh, G.; Wichrowski, N. J.; Evangelou, N.; Ghanekar, P. G.; Deshpande, S.; Kevrekidis, I. G.; Greeley, J. Active Learning of Ternary Alloy Structures and Energies. *npj Comput. Mater. 2024 101* **2024**, *10* (1), 1–11. https://doi.org/10.1038/s41524-024-01256-z.

(36) Back, S.; Yoon, J.; Tian, N.; Zhong, W.; Tran, K.; Ulissi, Z. W. Convolutional Neural Network of Atomic Surface Structures to Predict Binding Energies for High-Throughput Screening of Catalysts. *J. Phys. Chem. Lett.* **2019**, *10* (15), 4401–4408. https://doi.org/10.1021/acs.jpclett.9b01428.

(37) Shahriari, B.; Swersky, K.; Wang, Z.; Adams, R. P.; De Freitas, N. Taking the Human out of the Loop: A Review of Bayesian Optimization. *Proc. IEEE* **2016**, *104* (1), 148–175.

https://doi.org/10.1109/JPROC.2015.2494218.

(38) Kresse, G.; Furthmü, J. *Efficient Iterative Schemes for Ab Initio Total-Energy Calculations Using a Plane-Wave Basis Set*; 1996.

(39) Perdew, J. P.; Burke, K.; Ernzerhof, M. *Generalized Gradient Approximation Made Simple*; 1996.

(40) Monkhorst, H. J.; Pack, J. D. *Special Points for Brillonin-Zone Integrations**; 1976; Vol. 13.

(41) Blochl, P. E. *Projector Augmented-+rave Method*; Vol. 50.

(42) Methfessel, M.; Paxton, A. T. *High-Precision Sampling for Brillouin-Zone Integration in Metals*; Vol. 40.

(43) Hjorth Larsen, A.; JØrgen Mortensen, J.; Blomqvist, J.; Castelli, I. E.; Christensen, R.; Dułak, M.; Friis, J.; Groves, M. N.; Hammer, B.; Hargus, C.; Hermes, E. D.; Jennings, P. C.; Bjerre Jensen, P.; Kermode, J.; Kitchin, J. R.; Leonhard Kolsbjerg, E.; Kubal, J.; Kaasbjerg, K.; Lysgaard, S.; Bergmann Maronsson, J.; Maxson, T.; Olsen, T.; Pastewka, L.; Peterson, A.; Rostgaard, C.; SchiØtz, J.; Schütt, O.; Strange, M.; Thygesen, K. S.; Vegge, T.; Vilhelmsen, L.; Walter, M.; Zeng, Z.; Jacobsen, K. W. The Atomic Simulation Environment - A Python Library for Working with Atoms. *J. Phys. Condens. Matter* **2017**, *29* (27). https://doi.org/10.1088/1361-648X/aa680e.

(44) Ong, S. P.; Richards, W. D.; Jain, A.; Hautier, G.; Kocher, M.; Cholia, S.; Gunter, D.; Chevrier, V. L.; Persson, K. A.; Ceder, G. Python Materials Genomics (Pymatgen): A Robust, Open-Source Python Library for Materials Analysis. *Comput. Mater. Sci.* **2013**, *68*, 314–319. https://doi.org/10.1016/j.commatsci.2012.10.028.

(45) Deshmukh, G.; Wichrowski, N. J.; Evangelou, N.; Ghanekar, P. G.; Deshpande, S.; Kevrekidis, I. G.; Greeley, J. Active Learning of Ternary Alloy Structures and Energies. **2023**. https://doi.org/10.26434/CHEMRXIV-2023-XTMN0.

(46) Xie, T.; Grossman, J. C. Crystal Graph Convolutional Neural Networks for an Accurate and

Interpretable Prediction of Material Properties. *Phys. Rev. Lett.* **2018**, *120* (14), 145301. https://doi.org/10.1103/PhysRevLett.120.145301.

(47) Ducastelle, F. Order and Phase Staibility in Alloys 1994. 1994, pp 122–157.

(48) Sluiter, M. H. F.; Colinet, C.; Pasturel, A. Ab Initio Calculation of the Phase Stability in Au-Pd and Ag-Pt Alloys. *Phys. Rev. B - Condens. Matter Mater. Phys.* **2006**, *73* (17), 1–17. https://doi.org/10.1103/PhysRevB.73.174204.

(49) Abrikosov, ! A; Ruban, A. V; Skriver, H. L.; Johansson, B. Calculated Orientation Dependence of Surface Segregations in PtsoNiso. *Phys. Rev. B 50*.

(50) Cao, L.; Niu, L.; Mueller, T. Computationally Generated Maps of Surface Structures and Catalytic Activities for Alloy Phase Diagrams. *Proc. Natl. Acad. Sci. U. S. A.* **2019**, *116* (44), 22044–22051. https://doi.org/10.1073/pnas.1910724116.

(51) Gauthier, Y.; Baudoing, R.; Lundberg, M.; Rundgren, J. Surface-Sandwich Segregation and Multilayer Relaxation on Pt0.5Ni0.5(110) Measured by Low-Energy Electron Diffraction: An Observation of Face-Related Segregation Reversal. *Phys. Rev. B* **1987**, *35* (15), 7867–7878. https://doi.org/10.1103/PhysRevB.35.7867.

(52) Nørskov, J. K.; Bligaard, T.; Logadottir, A.; Bahn, S.; Hansen, L. B.; Bollinger, M.; Bengaard, H.; Hammer, B.; Sljivancanin, Z.; Mavrikakis, M.; Xu, Y.; Dahl, S.; Jacobsen, C. J. H. Universality in Heterogeneous Catalysis. *J. Catal.* **2002**, *209* (2), 275–278. https://doi.org/10.1006/JCAT.2002.3615.

(53) Nørskov, J. K.; Bligaard, T.; Rossmeisl, J.; Christensen, C. H. Towards the Computational Design of Solid Catalysts. *Nat. Chem.* **2009**, *1* (1), 37–46. https://doi.org/10.1038/nchem.121.

(54) Stephens, I. E. L.; Bondarenko, A. S.; Grønbjerg, U.; Rossmeisl, J.; Chorkendorff, I. Understanding the Electrocatalysis of Oxygen Reduction on Platinum and Its Alloys. *Energy Environ. Sci.* **2012**, *5* (5), 6744–6762. https://doi.org/10.1039/C2EE03590A.

(55) Strasser, P.; Koh, S.; Anniyev, T.; Greeley, J.; More, K.; Yu, C.; Liu, Z.; Kaya, S.; Nordlund,

D.; Ogasawara, H.; Toney, M. F.; Nilsson, A. Lattice-Strain Control of the Activity in Dealloyed Core–Shell Fuel Cell Catalysts. *Nat. Chem. 2010 26* **2010**, *2* (6), 454–460. https://doi.org/10.1038/nchem.623.

(56) Hansen, H. A.; Rossmeisl, J.; Nørskov, J. K. Surface Pourbaix Diagrams and Oxygen Reduction Activity of Pt , Ag and Ni(111) Surfaces Studied by DFT. *Phys. Chem. Chem. Phys.* **2008**, *10* (25), 3722–3730. https://doi.org/10.1039/B803956A.

(57) Ulissi, Z. W.; Singh, A. R.; Tsai, C.; Nørskov, J. K. Automated Discovery and Construction of Surface Phase Diagrams Using Machine Learning. *J. Phys. Chem. Lett.* **2016**, *7* (19), 3931–3935. https://doi.org/10.1021/ACS.JPCLETT.6B01254/SUPPL_FILE/JZ6B01254_SI_001.PDF.

TOC Figure